Supplementary Information

Self-standing porous intermetallic Fe_3Mn_7 phase as bifunctional electrocatalyst towards efficient overall water splitting

Yan Wen,*[a] Yu Cao,[b] Yufei Ren [c] and Zhen Huo *[d]

[a] Faculty of Chemical Engineering and Energy Technology, Shanghai Institute of Technology, Shanghai 201418, China

[b] Shanxi Zihuan Technology Co., Ltd., Taiyuan 030021, China

[c] School of Information and Communication Engineering, Hainan University, Haikou 570228, China

[d] Desion Engineering Company, China Chemical Engineering Second Construction Corporation, Taiyuan 030021, China

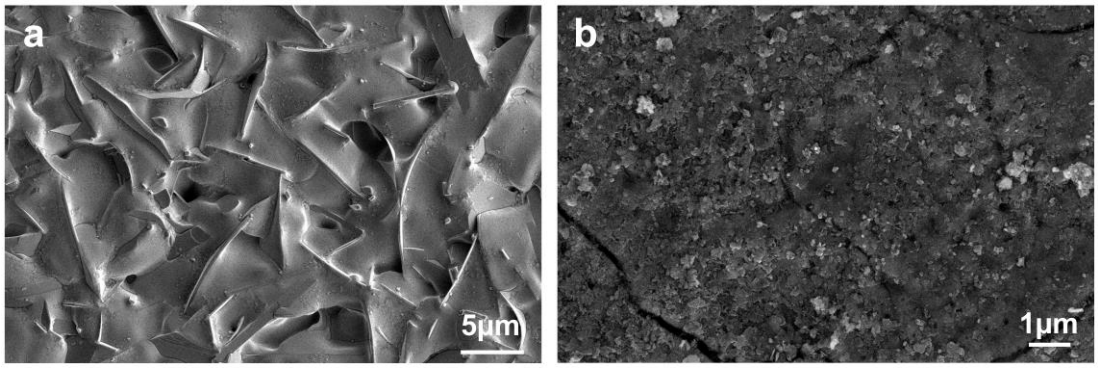

Fig. S1 SEM images of (a)D-MnNiFe-0 and (b) D-MnNiFe-60.

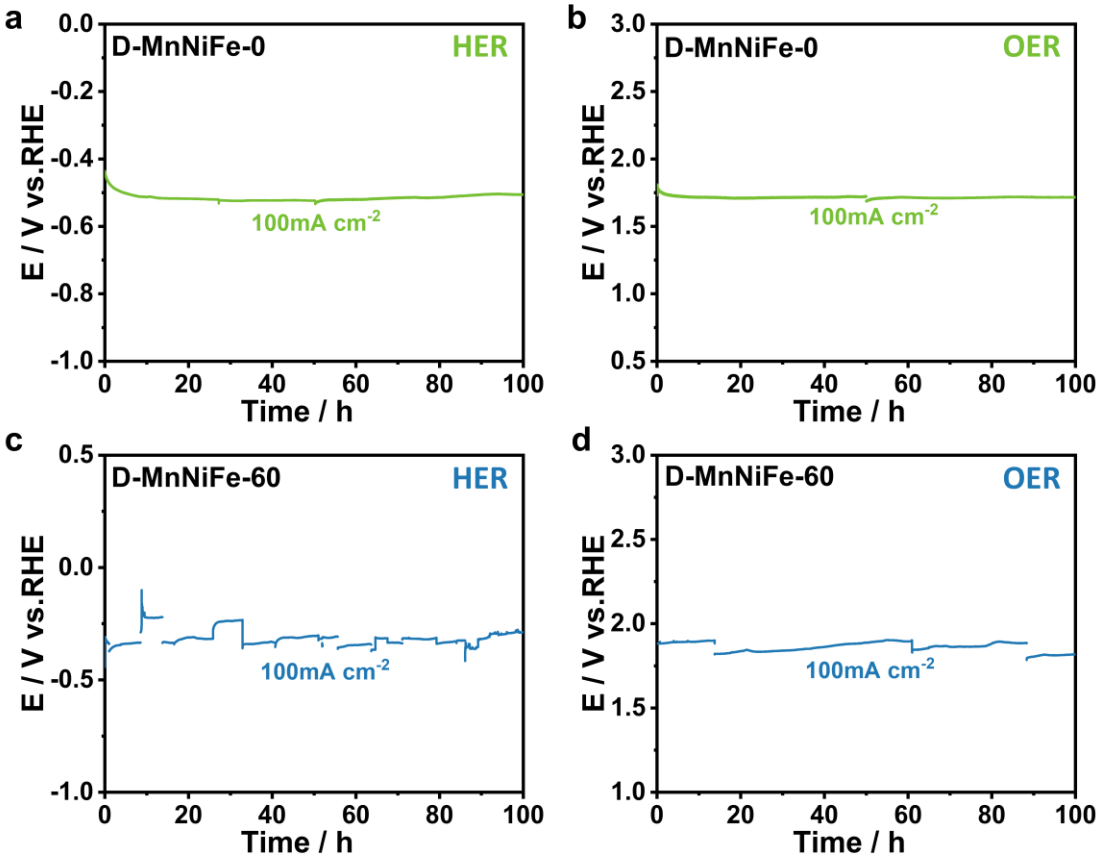

Fig. S2 CP profile of D-MnNiFe-0 and D-MnNiFe-60 for (a, c) HER and (b, d) OER at 100 mA cm^{-2} in 1.0 M KOH.

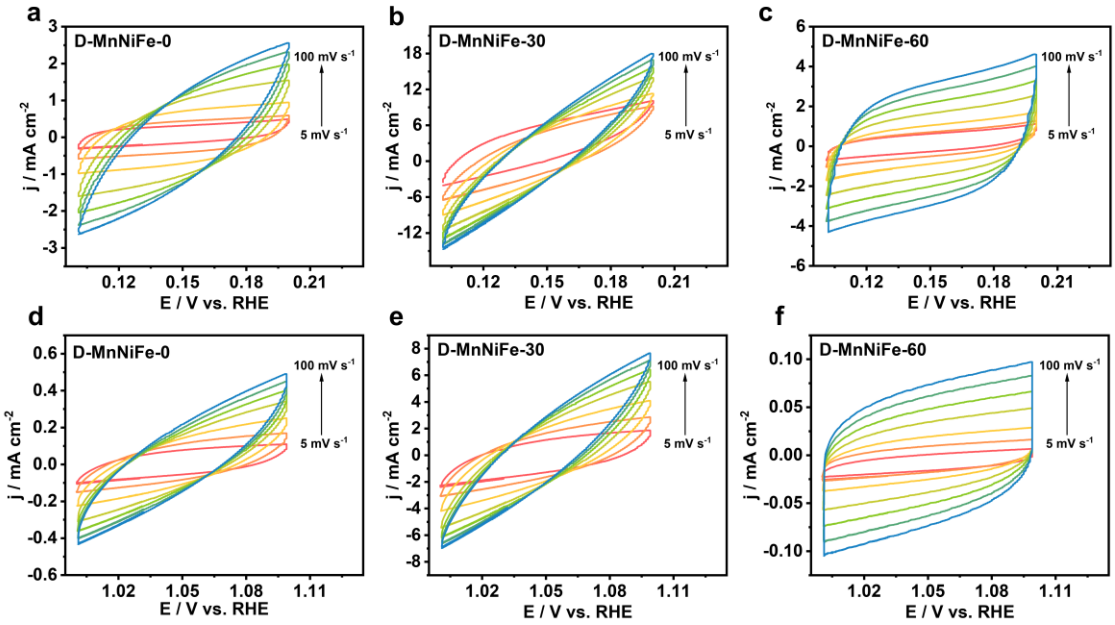

Fig. S3 CV curves for HER (0.1～0.2 V vs. RHE) of (a) D-MnNiFe-0, (b) D-MnNiFe-30 and (c) D-MnNiFe-60 electrodes under different scan rates; CV curves for OER (1.0～1.1 V vs. RHE) of (d) D-MnNiFe-0, (e) D-MnNiFe-30 and (f) D-MnNiFe-60 electrodes under different scan rates.

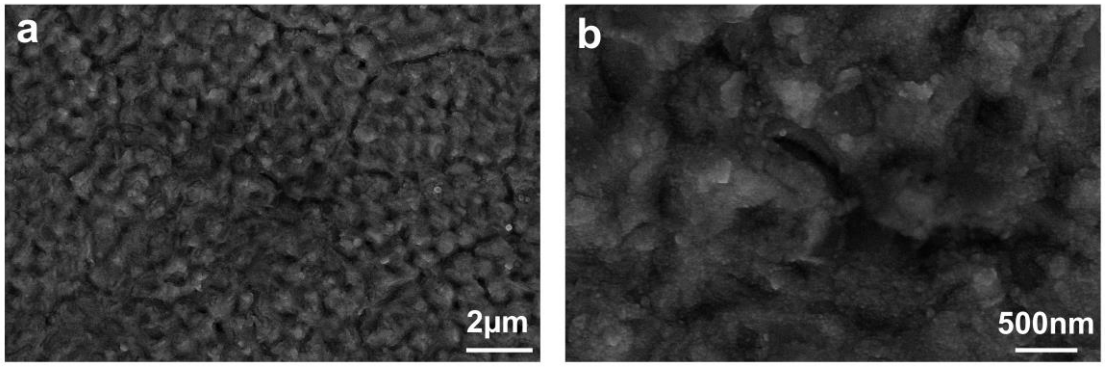

Fig. S4 (a) Low- and (b) high-magnification SEM images after stability testing in symmetric D-MnNiFe-30 || D-MnNiFe-30 electrodes

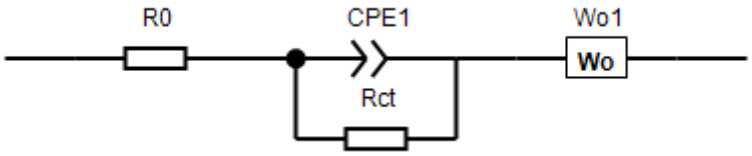

Fig. S5 Equivalent circuit diagram of EIS

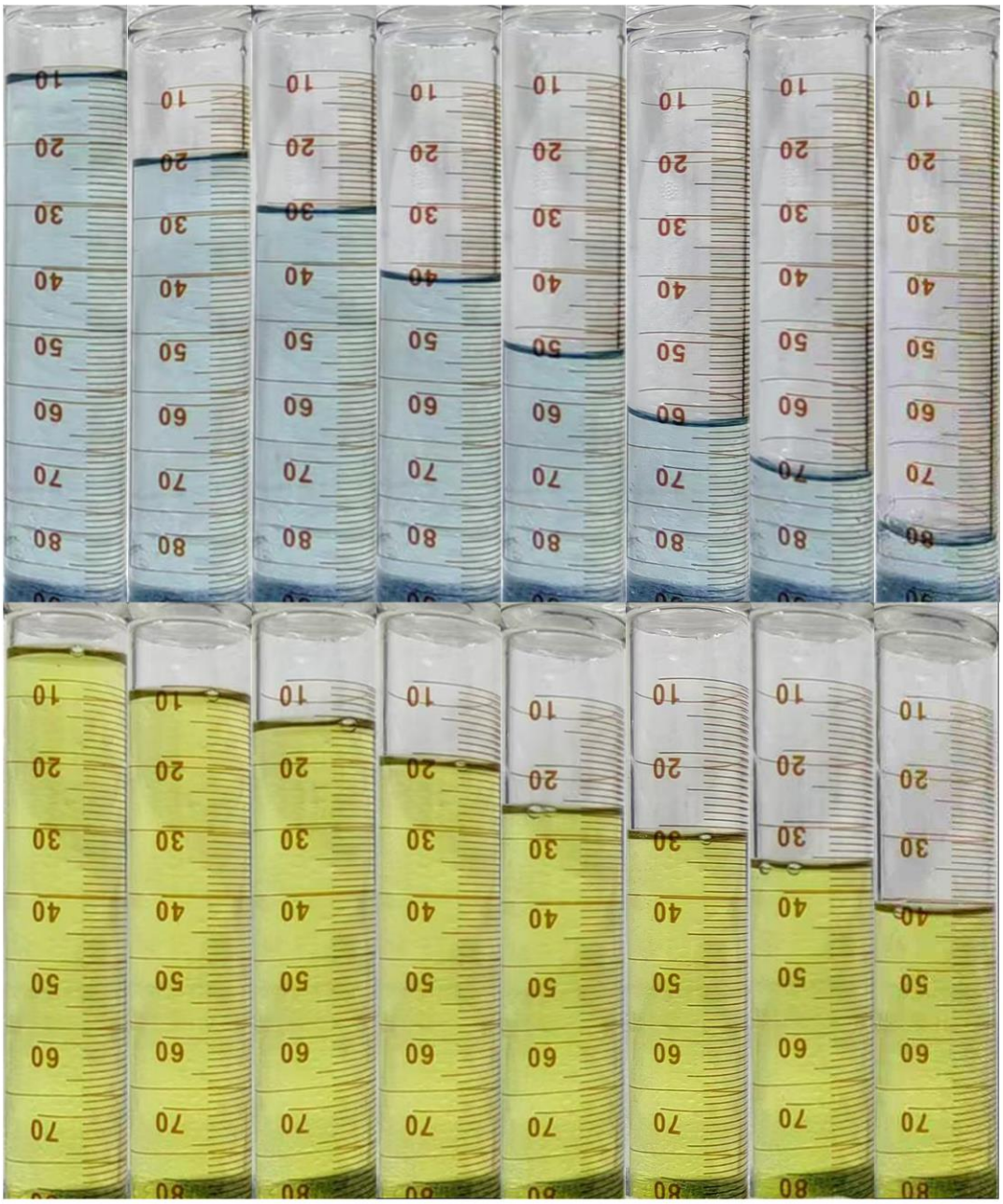

Fig. S6 photographs of H_2 (top) and O_2 (down) collected at 2 V for 80 min.

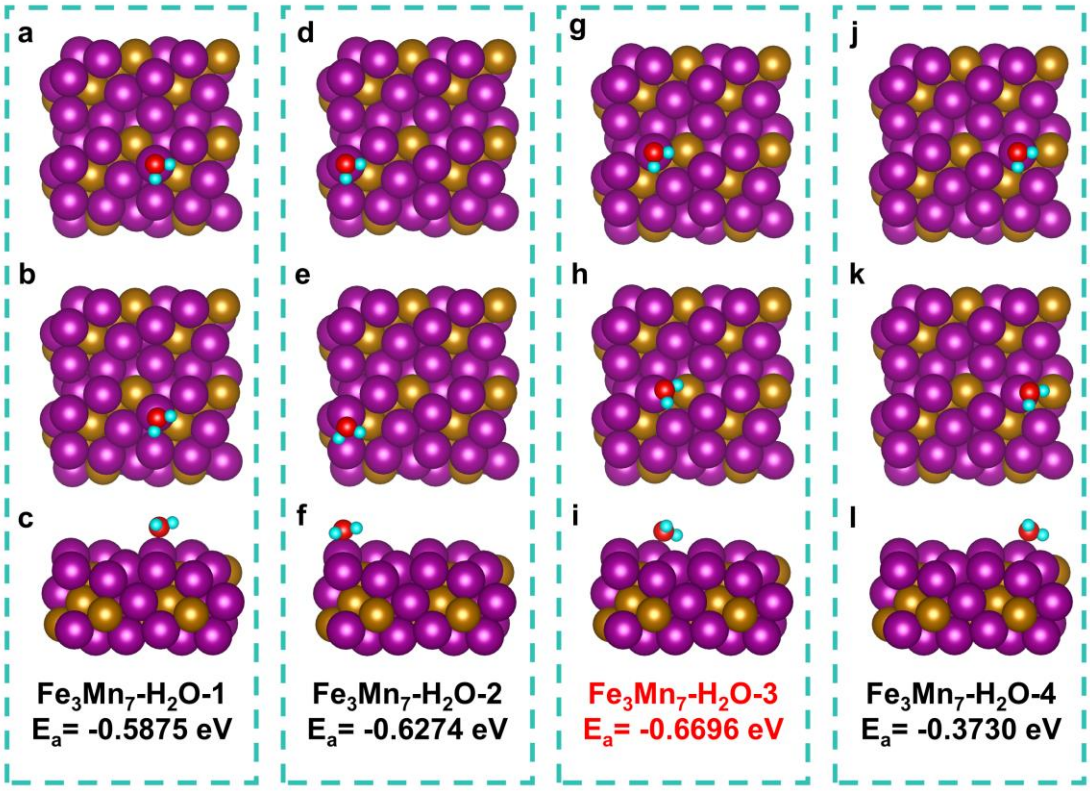

Fig. S7 (a, d, g, j) *H_2O adsorption models of Fe_3Mn_7 on different metal sites. (b, e, h, k) Top view of optimized *H_2O adsorption models. (c, f, i, l) Front view and corresponding adsorption energies of optimized *H_2O adsorption models.

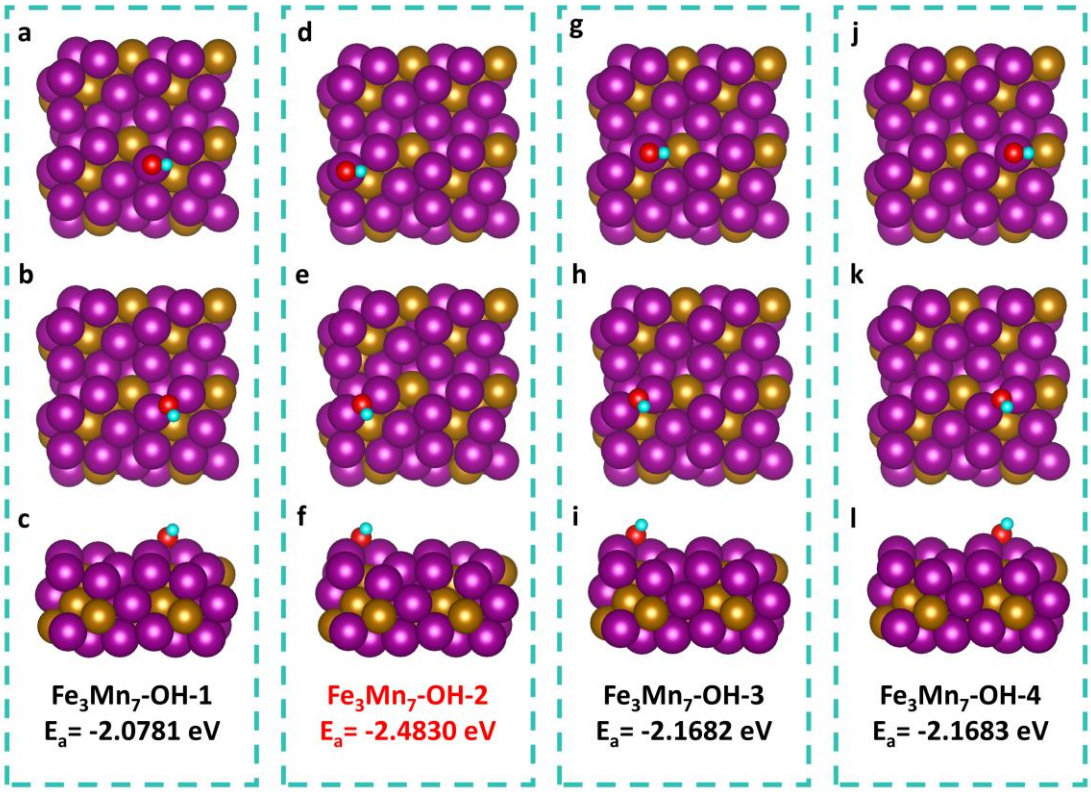

Fig. S8 (a, d, g, j) *OH adsorption models of Fe_3Mn_7 on different metal sites. (b, e, h, k) Top view of optimized *OH adsorption models. (c, f, i, l) Front view and corresponding adsorption energies of optimized *OH adsorption models.

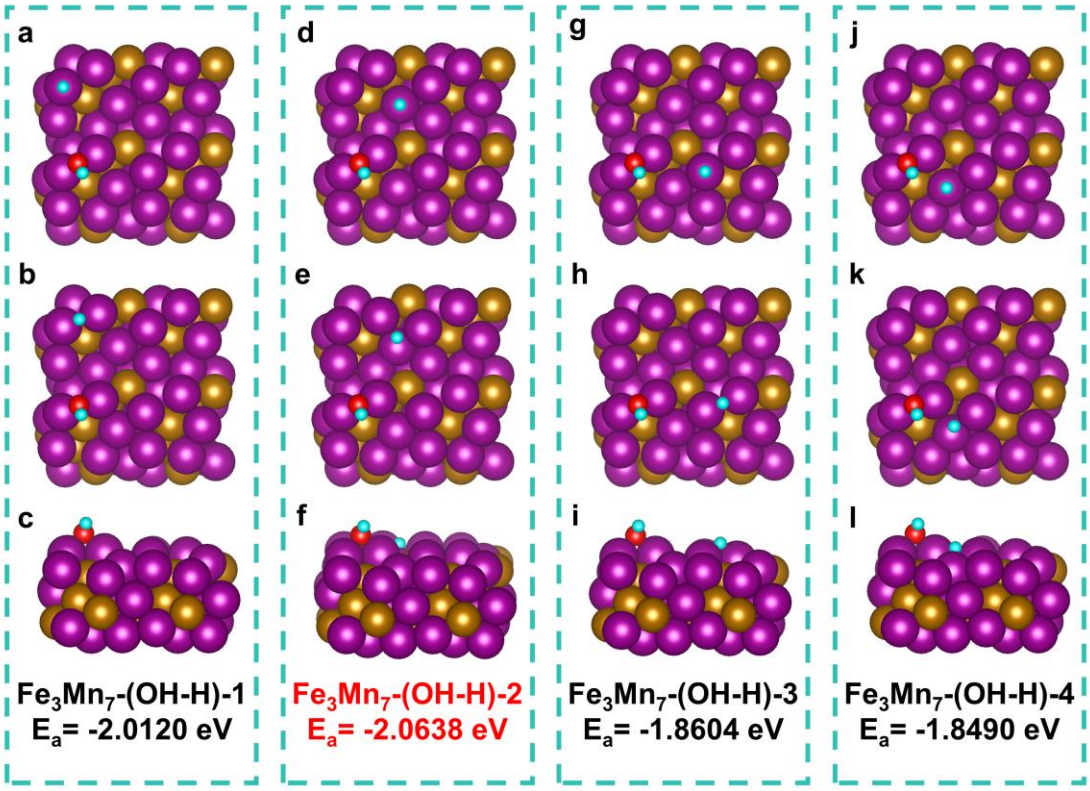

Fig. S9 (a, d, g, j) *(OH-H) adsorption models of Fe_3Mn_7 on different metal sites. (b, e, h, k) Top view of optimized *(OH-H) adsorption models. (c, f, i, l) Front view and corresponding adsorption energies of optimized *(OH-H) adsorption models.

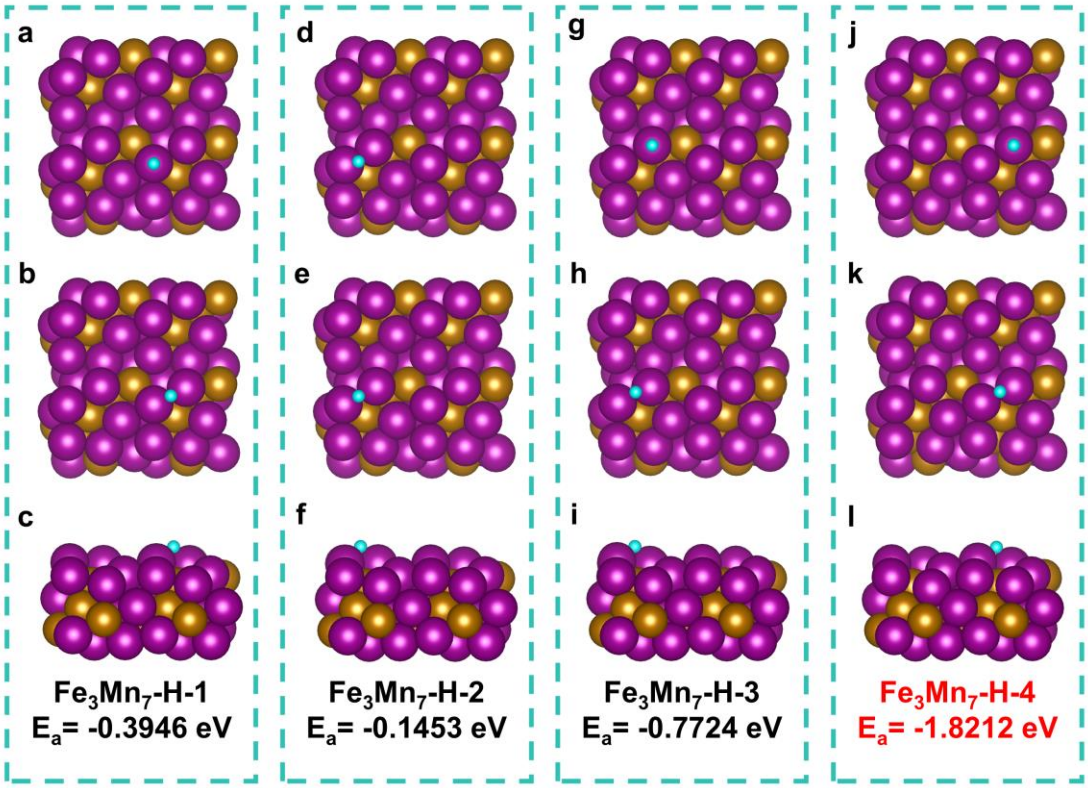

Fig. S10 (a, d, g, j) *H adsorption models of Fe_3Mn_7 on different metal sites. (b, e, h, k) Top view of optimized *H adsorption models. (c, f, i, l) Front view and corresponding adsorption energies of optimized *H adsorption models.

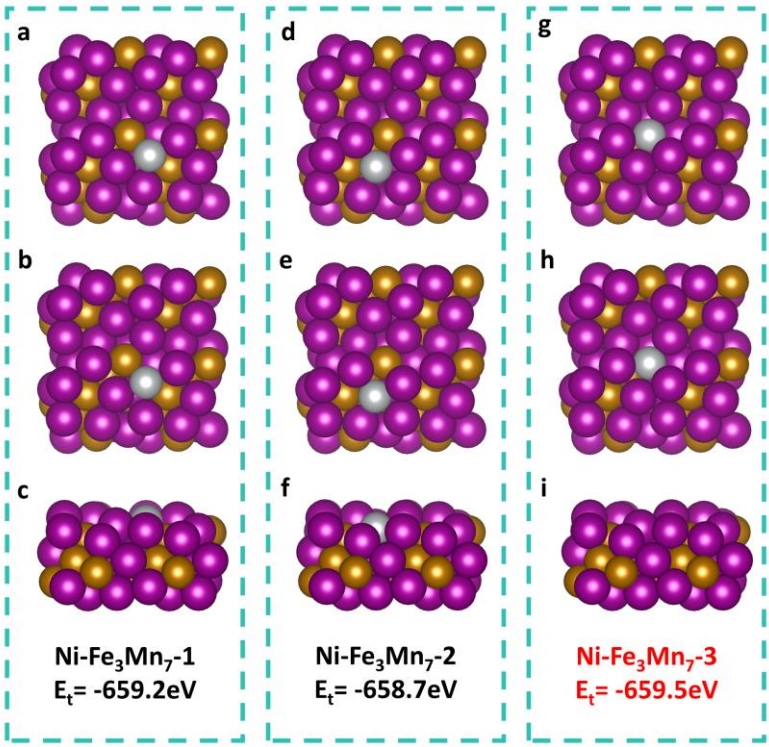

Fig. S11 (a, d, g) Top view of Ni-Fe_3Mn_7 models. (b, e, h) Top view of optimized Ni-Fe_3Mn_7 models. (c, f, i) Front view of optimized Ni-Fe_3Mn_7 models and corresponding total energies.

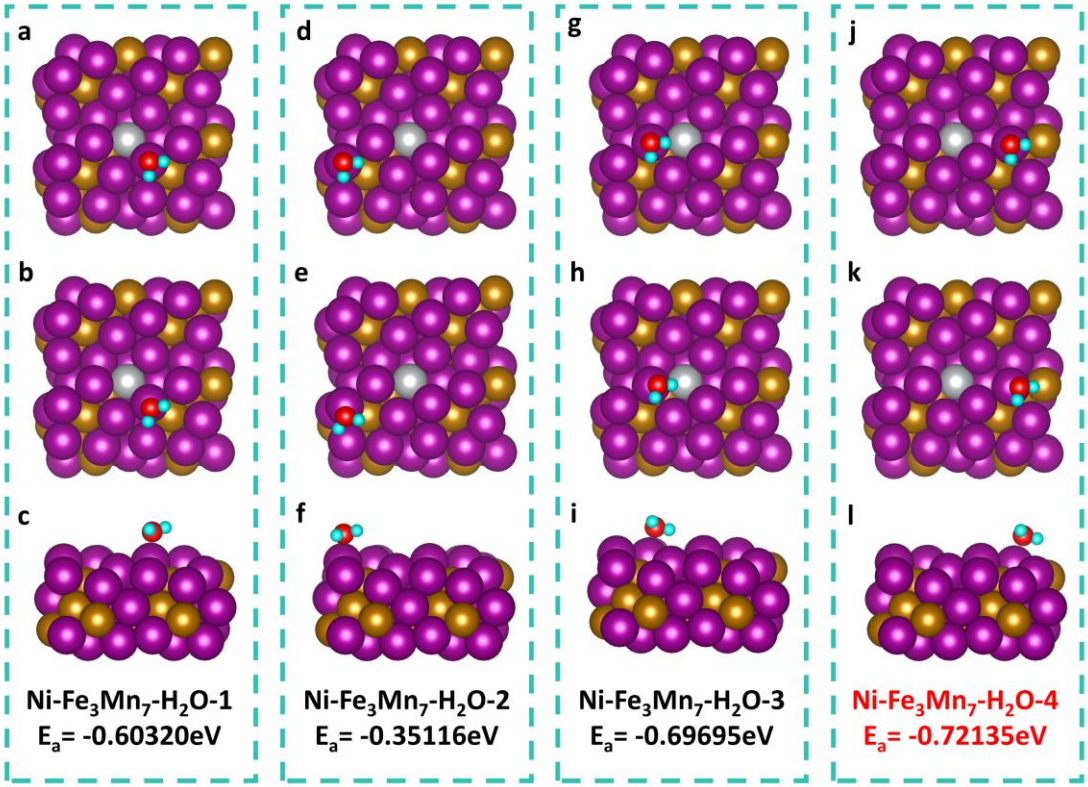

Fig. S12 (a, d, g, j) *H_2O adsorption models of Ni-Fe_3Mn_7 on different metal sites. (b, e, h, k) Top view of optimized *H_2O adsorption models. (c, f, i, l) Front view and corresponding adsorption energies of optimized *H_2O adsorption models.

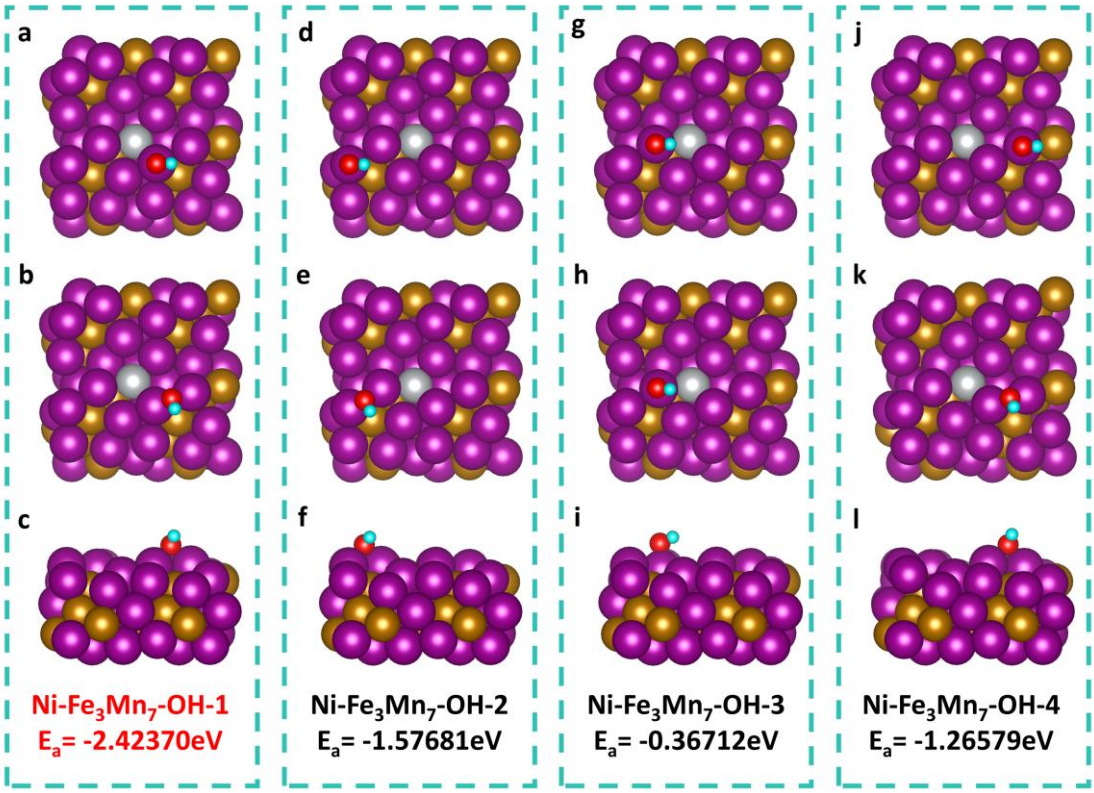

Fig. S13 (a, d, g, j) *OH adsorption models of Ni-Fe_3Mn_7 on different metal sites. (b, e, h, k) Top view of optimized *OH adsorption models. (c, f, i, l) Front view and corresponding adsorption energies of optimized *OH adsorption models.

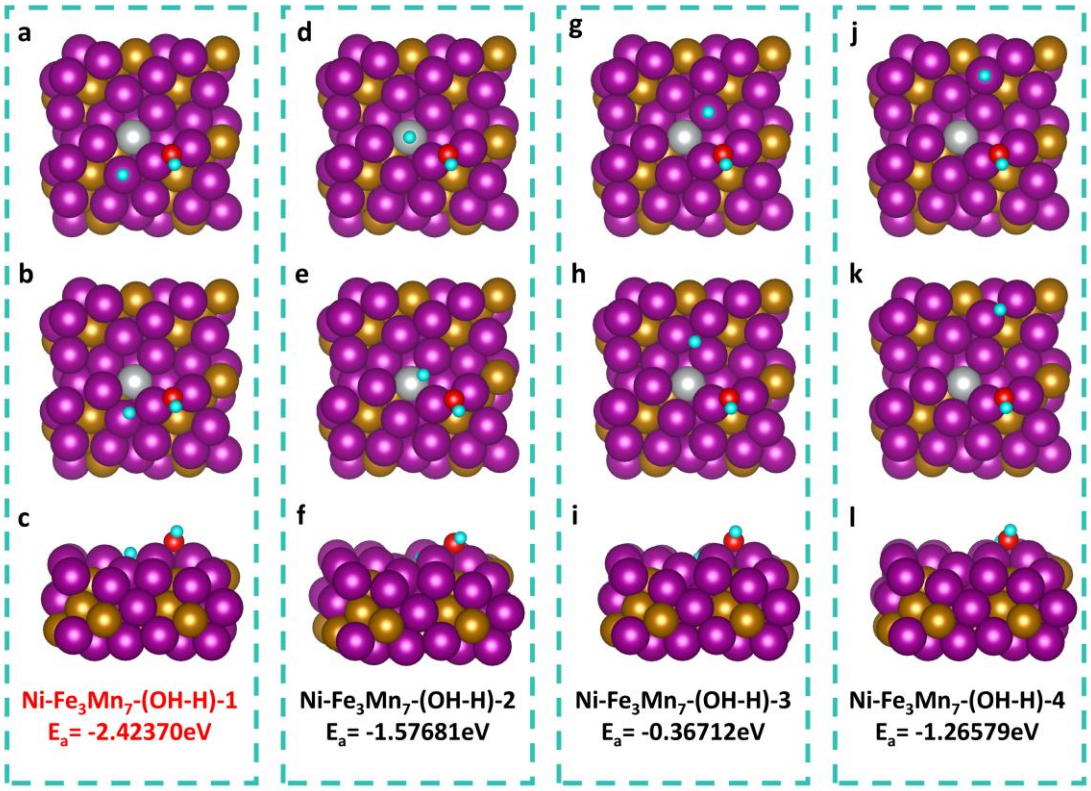

Fig. S14 (a, d, g, j) *(OH-H) adsorption models of Ni-Fe_3Mn_7 on different metal sites. (b, e, h, k) Top view of optimized *(OH-H) adsorption models. (c, f, i, l) Front view and corresponding adsorption energies of optimized *(OH-H) adsorption models.

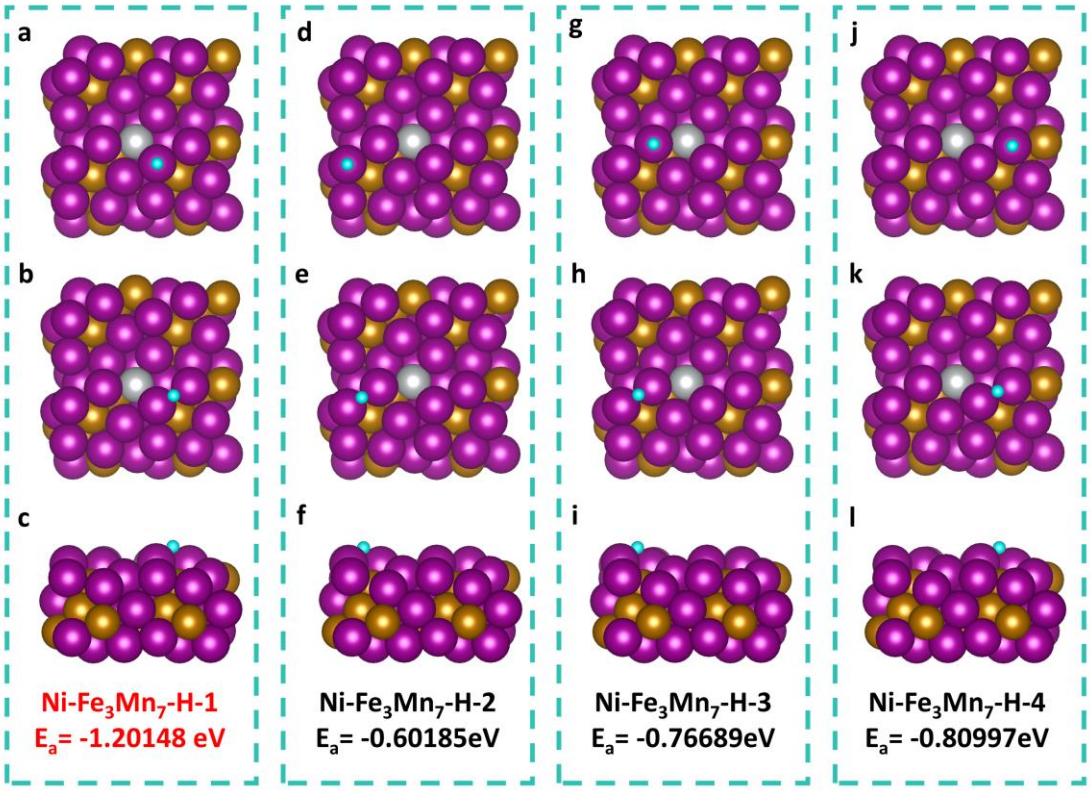

Fig. S15 (a, d, g, j) *H adsorption models of Ni-Fe_3Mn_7 on different metal sites. (b, e, h, k) Top view of optimized *H adsorption models. (c, f, i, l) Front view and corresponding adsorption energies of optimized *H adsorption models.

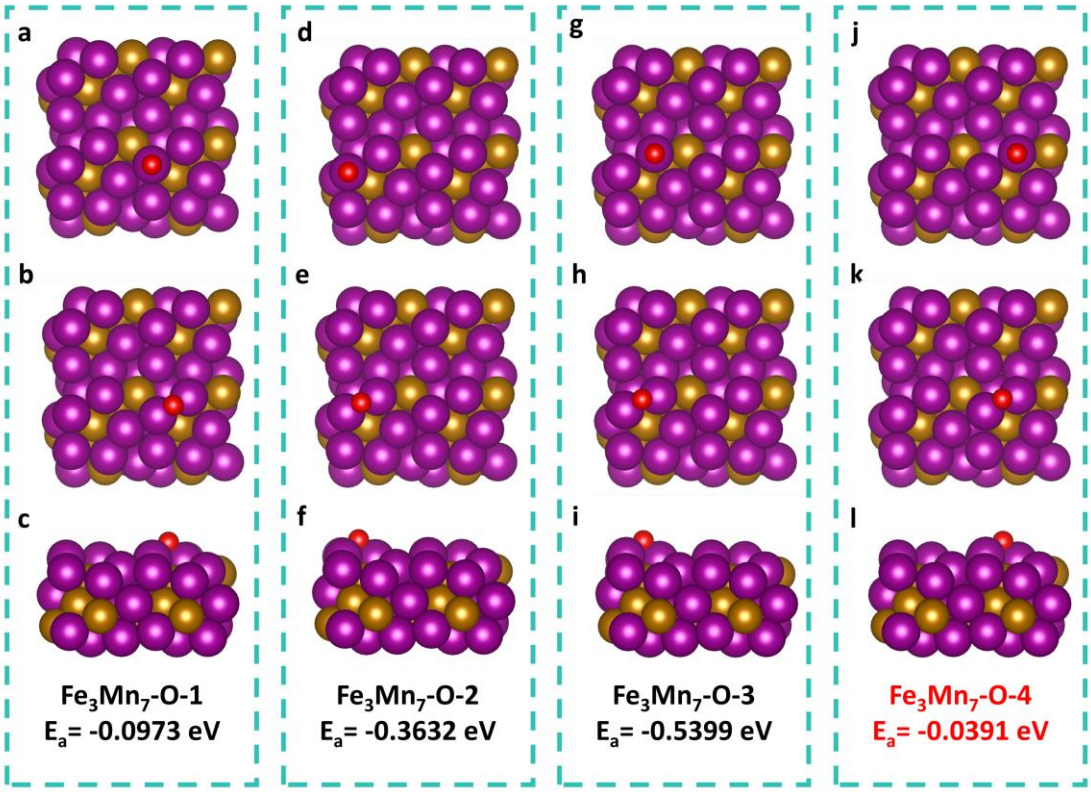

Fig. S16 (a, d, g, j) *O adsorption models of Fe_3Mn_7 on different metal sites. (b, e, h, k) Top view of optimized *O adsorption models. (c, f, i, l) Front view and corresponding adsorption energies of optimized *O adsorption models.

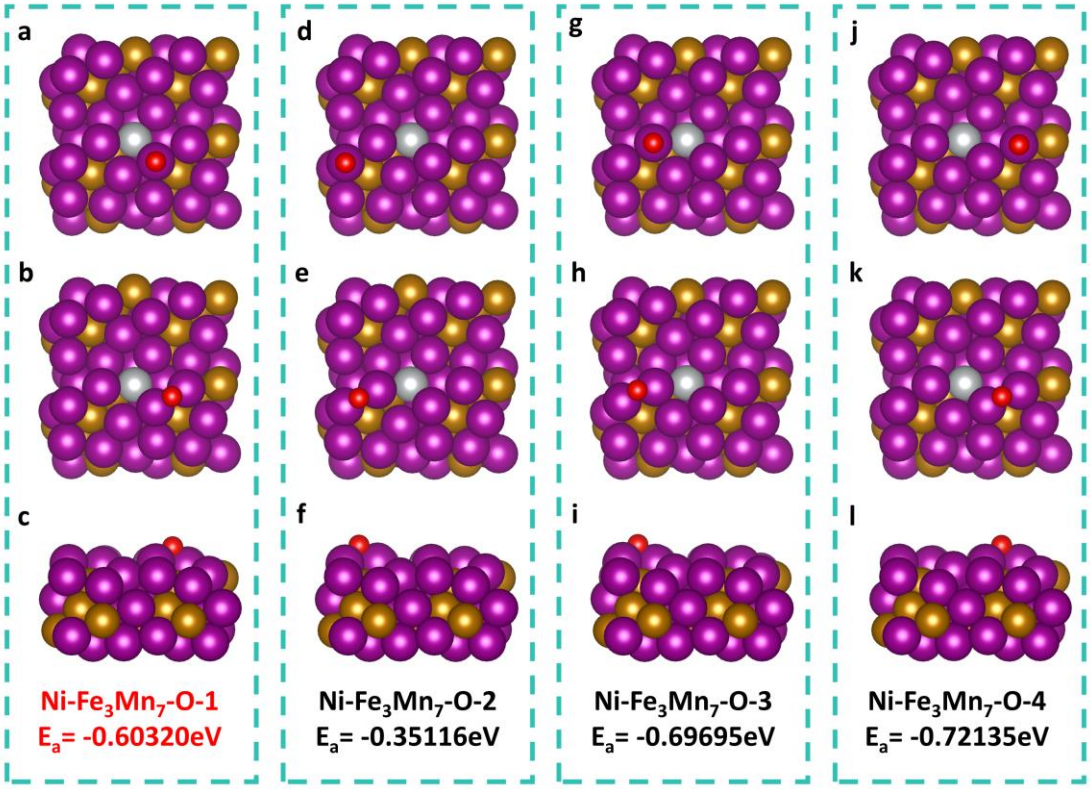

Fig. S17 (a, d, g, j) *O adsorption models of Ni-Fe_3Mn_7 on different metal sites. (b, e, h, k) Top view of optimized *O adsorption models. (c, f, i, l) Front view and corresponding adsorption energies of optimized *O adsorption models.

Table S1. Elemental compositions of D-MnNiFe-0, D-MnNiFe-30, and D-MnNiFe-60 determined by ICP-OES analysis.

Sample	Element	Content in sample (wt%)
D-MnNiFe-0	Mn	64.42
	Ni	11.24
	Fe	21.00
D-MnNiFe-30	Mn	49.85
	Ni	15.54
	Fe	25.03
D-MnNiFe-60	Mn	68.38
	Ni	10.82
	Fe	19.84

Table S2. XPS peak-fitting parameters for Fe, Mn, and Ni species in D-MnNiFe-30.

	Peak BE	Area	Area Ratio
Fe^{3+} $2p_{3/2}$	713.07	35226.14	18.68%
Fe^{2+} $2p_{1/2}$	724.23	20423.23	10.83%
Fe^{0} $2p_{3/2}$	707	26135.14	13.86%
Fe^{0} $2p_{1/2}$	719.72	20862.88	11.06%
Fe^{3+} $2p_{1/2}$	726.34	14767.58	7.83%
Sat. $2p_{1/2}$	733.82	3375.72	1.79%
Fe^{2+} $2p_{3/2}$	710.88	56299.42	29.85%
Sat. $2p_{3/2}$	715.81	11532.28	6.11%
Mn^{3+} $2p_{3/2}$	641.57	46650.27	18.95%
Mn^{2+} $2p_{3/2}$	640.41	44632.74	18.13%
Mn^{4+} $2p_{3/2}$	642.90	63224.59	25.68%
Mn^{0} $2p_{3/2}$	638.52	50629.51	20.57%
Mn^{0} $2p_{1/2}$	651.01	5078.23	2.06%
Mn^{2+} $2p_{1/2}$	652.09	7834.83	3.18%
Mn^{3+} $2p_{1/2}$	653.09	14950.43	6.07%
Mn^{4+} $2p_{1/2}$	654.27	13160.44	5.35%
Ni^{0} $2p_{3/2}$	852.18	50006.55	30.07%
Ni^{2+} $2p_{3/2}$	855.75	58716.35	35.31%
Ni^{0} $2p_{1/2}$	869.41	19988.52	12.02%
Sat. $2p_{3/2}$	861.17	7706.18	4.63%
Ni^{2+} $2p_{1/2}$	873.41	18962.38	11.40%
Sat. $2p_{1/2}$	878.99	10912.52	6.56%

Table S3. Fitted EIS parameters (R_s and R_{ct}) for the Catalysts under HER and OER conditions.

Catalysts	HER-R_s / Ω	HER-R_{ct} / Ω	OER-R_s / Ω	OER-R_{ct} / Ω
D-MnNiFe-0	0.726	13.632	1.2826	12.8
D-MnNiFe-30	0.604	2.484	0.57569	1.711
D-MnNiFe-60	1.330	46.419	0.87752	18.765

Table S4. Comparison of the electrochemical HER activities of this work with recent outstanding reported D-MnNiFe-30 electrocatalysts under 1M alkaline conditions.

Electrocatalyst	**η_{10} (mV)**	**Tafel slope (mV dec^{-1})**	**Reference**
D-MnNiFe-0	**166**	**107.5**	
D-MnNiFe-30	**32**	**54.1**	**This work**
D-MnNiFe-60	**148**	**60.9**	
P-CoN/CMO/Co_3O_4/NF	109	89.1	[1]
Pt–NiCoP/PRGF	56	59	[2]
Ag/NiFe-MOF-30	138	57.4	[3]
$FeNNi_3$/NF	57	109	[4]
$Co_{0.15}$@ARC	172	108	[5]
NCFP@LDH	46	65.95	[6]
HEA-AO	173	97.89	[7]
Ir@CoNi-BP900	67.7	59.34	[8]
CoO/CoP_3	205	137	[9]
RuFeNiCo-NC-3	60.7	51.9	[10]

Table S5. Comparison of the electrochemical OER activities of this work with recent outstanding reported D-MnNiFe-30 electrocatalysts under 1M alkaline conditions.

Electrocatalyst	**η_{10} (mV)**	**Tafel slope (mV dec^{-1})**	**Reference**
D-MnNiFe-0	**461**	**75.2**	
D-MnNiFe-30	**323**	**63.3**	**This work**
D-MnNiFe-60	**361**	**84.7**	
RuFeNiCo-NC-3	330	53.88	[10]
CV@MWCNT	337	80	[11]
Mn-$Co_{1.29}Ni_{1.71}O_4$	334.3	76.7	[12]
CoFe/$CoFe_2O_4$@NCNTs	344	143.8	[13]
LDH-A-Fe/NC-CNT	360	107	[14]
ZCO-C	330	59.7	[15]
n#CMS	345	80.89	[16]
FeCoNiCrZnCu	357	94	[17]
Fe_2Co/C	335	58.8	[18]
CuO/$CuNb_2O_6$	380	104	[19]

Table S6. AWE activities of D-MnNiFe-30 || D-MnNiFe-30 couple along with other reported catalysts under 1M alkaline conditions.

Couple	Cell voltage (V)	Condition	Reference
D-MnNiFe-30 || D-MnNiFe-30	**1.83V@100mA cm^{-2}**	**25℃ 1M KOH**	**This work**
$CoCrFeNiMoAl_{0.6}$ || $CoCrFeNiMoAl_{0.6}$	1.83V@100mA cm-2	25℃ 1M KOH	[20]
$NiSe_2$/CoSe/NF-3.0 || $NiSe_2$/CoSe/NF-3.0	1.85V@100mA cm-2	25℃ 1M KOH	[21]
$4N_6$Co-MoS_2 || $4N_6$Co-MoS_2	2.2V@100mA cm-2	25℃ 1M KOH	[22]
NiP-Fabric || NiP-Fabric	1.86V@100mA cm-2	25℃ 1M KOH	[23]
NCSO-60/NF || NCSO-60/NF	1.87V@100mA cm-2	25℃ 1M KOH	[24]

References

1 J. Ran, Z. Zhang, H. Feng, *et al., Int. J. Hydrogen Energy*, 2024, **64**, 935-946.
2 D. Li, F. Kong, B. Sun, *et al., Int. J. Hydrogen Energy*, 2025, **120**, 412-421.
3 C. Zhang, H. Chen, C. Zhou, *et al., ACS Appl. Nano Mater.*, 2025, **8**, 6897-6906.
4 A. Zhou, D. Song, Z. Hui, *et al., Results Phys.*, 2024, **59**, 107611.
5 Y. Zhou, Y. Luo, Q. Li, *et al., Energy Fuels*, 2024, **38**, 15560-15570.
6 X. Fu, H. Liao, Z. Zhang, *et al., Chem. Eng. J.*, 2025, **505**, 159520.
7 Y.X. Yu, J.L. Xu, L.W. Zhang, *et al., Int. J. Hydrogen Energy*, 2024, **72**, 209-219.
8 L. Zhu, Y. Cheng, Y. Gong, *Int. J. Hydrogen Energy*, 2025, **97**, 1177-1186.
9 Y. Luo, G. Zhang, Y. Wang, *et al., Sep. Purif. Technol.*, 2025, **363**, 132318.
10 Q. Lei, K. Zhu, L. Zuo, *et al., Mater. Sci. Eng. B*, 2024, **314**, 118036.
11 V. Singh, S. Singh, V. Rathour, *et al., ACS Appl. Eng. Mater.*, 2025, **3**, 672-683.
12 Y. Cheng, X. Guo, Z. Ma, *et al., Molecules*, 2025, **30**, 1162.
13 Z. Zhang, M. Yan, Z. Xiong, *et al., J. Energy Storage,* 2024, **101**, 113668.
14 W.H. Wang, C.H. Han, W.X. Hong, *et al., J. Energy Storage*, 2024, **85**, 111058.
15 G. Arulprakash, A. Kareem, S. Sellappan, *et al., Int. J. Hydrogen Energy*, 2024, **66**, 625-635.
16 T. Zeng, J. Lin, B. Wang, *et al., Chem. Eng. J.*, 2024, **500**, 156788.
17 M. Li, X. Ye, S. Guo, *et al., Int. J. Hydrogen Energy*, 2025, **130**, 644-653.
18 J. Guo, Y. Gao, X. Cao, *et al., Inorg. Chem. Commun.*, 2024, **170**, 113394.
19 H.P.A. Alves, T.O. Pereira, R.A. Raimundo, *et al., J. Phys. Chem. Solids*, 2025, **199**, 112525.
20 Y. Sun, F. Yang, S. Sun, *et al., J. Colloid Interface Sci.*, 2025, **684**, 1-10.
21 X. Huo, Y. Zhang, G. Zhou, *et al., J. Alloys Compd.*, 2025, **1026**, 180461.
22 X. Zhao, Z. Shang, N. Li, *et al., J. Colloid Interface Sci.*, 2025, **693**, 137642.
23 P.J. Sharma, K.H. Modi, P. Sahatiya, *et al., Appl. Surf. Sci.*, 2024, **644**, 158766.
24 S. Rajalekshmi, L. Kanishga, S.M. Senthil Kumar, *et al., J. Power Sources*, 2025, **657**, 238182.